Patch antenna terahertz photodetectors

D. Palaferri,[1] Y. Todorov,[1,a)] Y. N. Chen,[1] J. Madeo,[1,b)] A. Vasanelli,[1] L. H. Li,[2] A. G. Davies,[2] E. H. Linfield,[2] and C. Sirtori[1]
[1]*Laboratoire Matériaux et Phénomènes Quantiques, Université Paris Diderot, Sorbonne Paris Cité, CNRS-UMS 7162, 75013 Paris, France*
[2]*School of Electronic and Electrical Engineering, University of Leeds, Leeds LS2 9JT, United Kingdom*

(Received 10 March 2015; accepted 10 April 2015; published online 21 April 2015)

We report on the implementation of 5 THz quantum well photodetector exploiting a patch antenna cavity array. The benefit of our plasmonic architecture on the detector performance is assessed by comparing it with detectors made using the same quantum well absorbing region, but processed into a standard 45° polished facet mesa. Our results demonstrate a clear improvement in responsivity, polarization insensitivity, and background limited performance. Peak detectivities in excess of 5×10^{12} cmHz$^{1/2}$/W have been obtained, a value comparable with that of the best cryogenic cooled bolometers.
[http://dx.doi.org/10.1063/1.4918983]

Optoelectronic devices that operate in the terahertz (THz) frequency range (0.1–10 THz) have been receiving growing attention from many independent fields.[1,2] While the development of efficient sources has been particularly underpinned by recent advances in THz quantum cascade lasers,[3–5] on the detection side there is no dominant solution and therefore different approaches are still explored[6] such as thermal detectors (pyroelectric crystals, semiconductor, and hot electron bolometers[7]) and photoconductive detectors. THz Quantum Well Infrared Photo-detectors (QWIP) have been shown to be a valid solution to the demand of fast and high sensitive detection.[8–13] These devices use intersubband (ISB) transitions in a semiconductor QW superlattice (mainly n-type doped GaAs/AlGaAs) to generate photocurrent, in a similar manner to their mid-infrared counterparts.[10,14] Several different geometries have been realized to couple light into THz QWIPs, in order to fulfill the ISB polarization selection rule:[15] these include via substrate coupling through a 45° polished facet,[8,14] diffraction gratings,[13,16,17] and metamaterials.[18] Recently, we demonstrated an antenna-coupled microcavity geometry for QWIPs operating at a wavelength of 9 μm which enables an improved light coupling, a reduced dark current, and a higher temperature performance.[19] In this paper, we report a similar realization for THz devices, where the operating temperature, usually limited to just 10 K,[8,10] is a critical issue for applications. In addition to the increased background limited performance of our detector architecture, from 13 K (Ref. 8) to 21 K, we achieve an approximately one order of magnitude improvement in the device detectivity, owing to improved collection efficiency and reduced dark current.

In our implementation, depicted in Figure 1, the QWIP devices are embedded in a double-metal structure, with the top surface patterned into an array of metallic patch antennas.[20,21] The lateral size of the patch s is set so that the fundamental TM_{100}/TM_{010} cavity modes are resonant with the ISB transition energy.[19,20,22] Because of the increased photonic confinement engendered by this technique, similar plasmonic devices have previously been employed with highly doped QWs to study the strong light-matter interaction in the THz range.[23] In the present work, we exploit the property of these structures to act as patch antennas; they couple in normal incident radiation, and collect photons over an area larger than that of the device itself, thus allowing a reduction in the dark current. The gain in the detector performance is confirmed by a direct comparison with the same QW structures processed into a substrate-coupled 45° facet geometry.[15]

Our device is based on an MBE (molecular beam epitaxy) grown structure, similar to sample v266 of Ref. 8: 20 GaAs QWs, each with a thickness $L_{QW} = 15.5$ nm and n doped across the central 10 nm regions with Si at a density of $N_d = 6.0 \times 10^{16}$ cm^{-3}, alternate with layers of AlGaAs (3% Al mole fraction) each with a thickness $L_b = 70.0$ nm. At the top and the bottom of this periodic structure, there are GaAs contact layers doped $N_d = 1.0 \times 10^{18}$ cm^{-3}, each having a thickness $L_c = 100.0$ nm.

The 45° facet substrate-coupled geometry consists of a 400×400 μm^2 square mesa, with annealed Pd/Ge/Ti/Au as a top contact and annealed Ni/Ge/Au/Ni/Au as a bottom contact. The patch-antenna devices shown in Figure 1 were

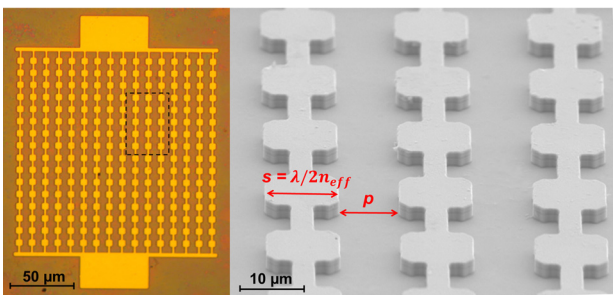

FIG. 1. Optical microscope (left) and scanning electron microscope (right) images of the 9 μm cavity array detector with indications of the main parameters of the array.

a)Author to whom correspondence should be addressed. Electronic mail: yanko.todorov@univ-paris-diderot.fr
b)Present address: Okinawa Institute of Science and Technology Graduate University, 1919-1 Tancha, Onna, Japan.

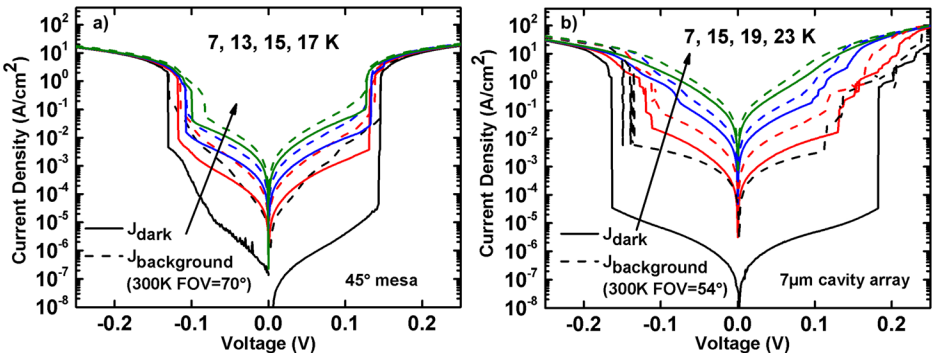

FIG. 2. IV characteristics of (a) the 45° mesa device, and (b) of the 7 μm antenna device, as a function of increasing temperature indicated by the arrow. Continuous lines show the dark current density and dashed lines show the background current density, the latter measured with a FOV = 70° (in (a)) and FOV = 54° (in (b)).

realized by optical lithography with annealed Pd/Ge/Ti/Au as both top and bottom contacts. The top surface is patterned into array of square microcavities, each electrically connected by strips 2 μm wide and 10 μm long. Four devices with different patch lengths of side s were tested: 6 μm, 7 μm, 8 μm, and 9 μm. The resonant frequency ν_{res} of the cavity is given[19,20,22] by $\nu_{res} = c/2n_{\text{eff}}s$, where n_{eff} is the effective index of the TM_{100}/TM_{010} mode, slightly higher than the index of the bulk GaAs.[22] Each cavity array consists of a 300×300 μm^2 size chip, with an array unit cell $\Sigma = (s+p)^2$, where $p = 10$ μm is the separation distance between two neighboring patches, and the total number of patches is N_{array}. The four devices tested have the following characteristics: $\Sigma = 256$ μm^2, $N_{array} = 361$, ($s = 6$ μm); $\Sigma = 289$ μm^2, $N_{array} = 324$,($s = 7$ μm); $\Sigma = 324$ μm^2, $N_{array} = 289$, ($s = 8$ μm); and $\Sigma = 361$ μm^2, $N_{array} = 256$, ($s = 9$ μm), so that the total area $N_{\text{array}} \times \Sigma$ is kept approximately constant. For all devices, the semiconductor region not covered by the metal is etched down to the 100 nm bottom contact layer, as shown in Figure 1.

Current-voltage (IV) profiles were measured on all samples (microcavities and 45° facet mesa) for temperatures ranging from 4 K to 300 K. The IV characteristics of the 45° facet sample and of the $s = 7$ μm antenna are shown in Figures 2(a) and 2(b), respectively. The continuous lines are dark current characteristics with the detector completely closed with a cryo-shield at the indicated temperatures. The dashed lines are IV characteristics under background (300 K) illumination on the detector, through an opening in the cryo–shield (always kept at the same temperature as the detector) in such a way that the field of view (FOV) is 70° for the 45° facet mesa and 54° for the $s = 7$ μm patch antenna array. In the cavity array device, the dark current density is obtained by taking into account the area of the metal pattern (see Figure 1), including cavities, wires, and pads; the photocurrent component of the background current has been normalized only by the area of the cavities, which is the only place where photocurrent is generated. All the IV characteristics (Fig. 2) present a step in current at a bias between 0.1 and 0.2 V (Fig. 2). This phenomenon has been explained by space charge accumulation and an impact ionization process where carriers are scattered directly into the QW continuum.[24,25]

The structures were further characterized through measurement of reflectivity and photocurrent spectra (Figure 3). Data were taken using a Bruker Fourier transform interferometer (FTIR) in a rapid scan mode. Reflectivity spectra (Fig. 3(a)) were recorded with an incident angle of 15° with respect to the array normal, and under no applied bias at 300 K. Besides the main cavity absorption peaks with frequencies ν_{res} between 4 THz and 6.5 THz depending on the patch size, we also observe a narrow replica around 9 THz. This replica corresponds to the interaction between the cavity mode and the GaAs optical phonons.[26] The observed resonances are phonon-polariton states resulting from the photon-phonon interaction. The shaded region (8–9THz) in Figure 3 is the GaAs Reststrahlen band which corresponds to the forbidden gap of the polariton dispersion.[26]

The photocurrent spectra are shown in Fig. 3(b) for the cavity devices and in Fig. 3(c) for the 45° facet mesa device. These spectra were recorded at 4 K and at a bias of 0.1 V, just before the current jump in the IV characteristics. The mesa device displays the typical broad shape of bound-to-quasi-continuum THz QWP, as reported in Ref. 8, with a frequency peak at 5.4 THz. The increased photocurrent signal at 9 THz is attributed to the increased density of states owed to the zero-group velocity of the upper phonon-polariton branch. Since the light-coupling into this structure is frequency independent these spectra can be considered to be the intrinsic photo-response of the QWs. Instead, for the case of the antenna coupled devices (Fig. 3(b)), the photocurrent peak always appears at the same position as set by the cavity

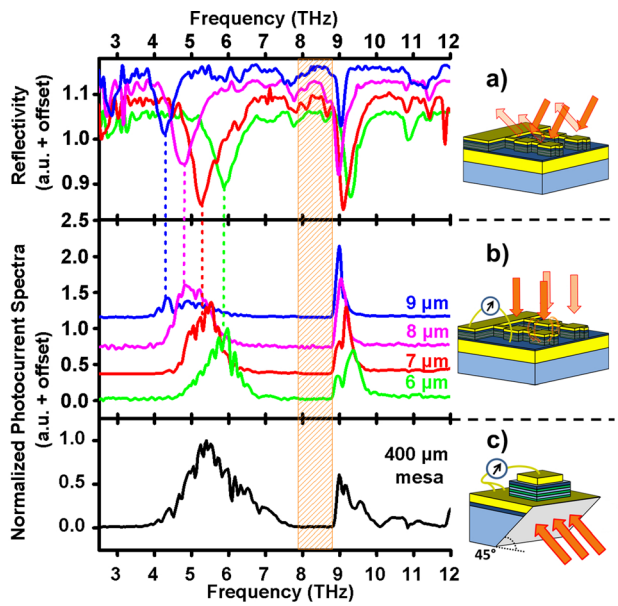

FIG. 3. (a) Reflectivity spectra of the cavity array detector. (b) and (c) photocurrent spectra of the cavity array and of the 45° mesa devices, respectively. The dashed area represents the GaAs Reststrahlen band.

mode, in exact correspondence with the reflectivity minima as shown in the upper panel of Fig. 3. As expected the photo-current decreases when the cavity is detuned from the maximum of the mesa photo-response at 5.4 THz. The $s = 7\,\mu$m antenna device is resonant with the intrinsic photo-response, while the $s = 9\,\mu$m is redshifted, resulting in cavity mode at lower energies than the intersubband absorption edge. This decreases the photo-detected signal (Fig. 3(b)).

In order to quantify the impact of the cavity array geometry on the device performance, we carried out systematic comparison between the responsivities of the 45° facet mesa device and the resonant $s = 7\,\mu$m sample. Responsivity measurements were performed using a calibrated 500 K blackbody. The out-coming THz radiation was focused on the sample through a pair of parabolic mirrors and chopped at 87 Hz, and the photon flux was estimated as the difference between blackbody sources at 500 K and 300 K and using the Planck's radiation law.[27] The photocurrent was recorded using a lock-in amplifier and a trans-impedance amplifier.

The responsivities are reported in Figure 4(a) as a function of the bias voltage and Figure 4(b) showing the photocurrent densities. In these measurements, the FOV of the source was imposed by the *f1* parabolic mirrors (*f1* indicates the ratio focal length over mirror diameter equal to 1) and is identical for both the cavity array and mesa devices. The responsivity of the 45°-facet mesa shows values up to 1 A/W in accordance with the results reported in Ref. 8. The linear responsivity as a function of bias confirms a bound-to-quasi-continuum transition[28] over this voltage range. For the $s = 7\,\mu$m device, we observe a four-fold enhancement of the responsivity, with values up to 5.5 A/W in negative bias. The photocurrent density of the array (Fig. 4(b)) is enhanced by a factor of 10, proving the enhanced collection efficiency owing to the antenna effect.

The overall peak responsivities of the two types of devices can be modeled with the following expressions that take into account the photoconductive gain g of the detector media, the ISB energy $E_{21} = 22.3$ meV (5.4 THz, this value also includes corrections due to many-body effects[9]), and parameters that describe the specific geometry of the detector[19,29,30]

$$R_{mesa}(E_{21}) = \frac{eg}{E_{21}} T \xi_{mesa} \eta_{isb}, \tag{1a}$$

$$R_{array}(E_{21}) = \frac{eg}{E_{21}} C \xi_{array} \frac{A_{isb}}{A_{isb} + 1/Q_{cav}}. \tag{1b}$$

Equation (1a) describes the responsivity of the 45° mesa-coupled geometry, where e is the electron charge, $T = 0.64$ is the facet transmission (light at normal incidence to the facet), and $\xi_{\mathrm{mesa}} = 0.5$ takes into account the polarization selection rule (only one polarization of the incident non-polarized radiation interacts with the QWs).[15] The quantity η_{isb} is the absorption quantum efficiency as defined in Ref. 15. Using the nominal parameters of our 20 QW structure we estimate $\eta_{isb} = 5.15\%$. From these numbers and the responsivity data in Fig. 4(a), we obtain the photoconductive gain g of the 45°-mesa device which is plotted in Fig. 4(c) (circles).

Equation (1b) is the overall responsivity peak of the cavity array, as established in Ref. 19. The coefficient C is the contrast of the reflectivity dip in Figure 3(a), and the polarization coefficient of the array is $\xi_{\mathrm{array}} = 70\%$ measured on the 7 μm antenna with a wire grid polarizer. This value is already better than the substrate coupled geometry, even though we would expect a value of 100% for a square patch.[22] However, in the present geometry part of the light is reflected because of the polarizing effect of the 2 μm-thick connecting wires (Fig. 1). The branching ratio $A_{\mathrm{isb}}/(A_{\mathrm{isb}} + 1/Q_{\mathrm{cav}})$ quantifies the detector absorption in the array geometry,[19] where Q_{cav} is the cavity quality factor, measured for cavities detuned from the ISB absorption peak.[20] The dimensionless quantity A_{isb} provides the ISB absorption coefficient for the array geometry at the cavity resonance $E_{\mathrm{cav}} = h\nu_{res}$ (h is the Planck's constant), and is described with a Lorentzian profile[19] $A_{\mathrm{isb}}(E_{\mathrm{cav}}) = A_{\mathrm{isb0}}/(1 + 4(E_{\mathrm{cav}} - E_{21})^2/\Gamma_{\mathrm{isb}}{}^2)$ with $A_{\mathrm{isb0}} = f_w E_p{}^2/(E_{21}\Gamma_{\mathrm{isb}})$. Here, $f_w = L_{\mathrm{QW}}/(L_{\mathrm{QW}} + L_b) = 0.16$ is the overlap factor between the cavity mode and the absorbing region (including the contact layers) $E_p = 7$ meV is the ISB plasma energy,[31,32] and $\Gamma_{\mathrm{isb}} = 4.2$ meV is the FWHM of the ISB peak extracted from a Lorentzian fit of the high energy part of the mesa photo-response (Fig. 3(c)). The values of these parameters for different gratings have been

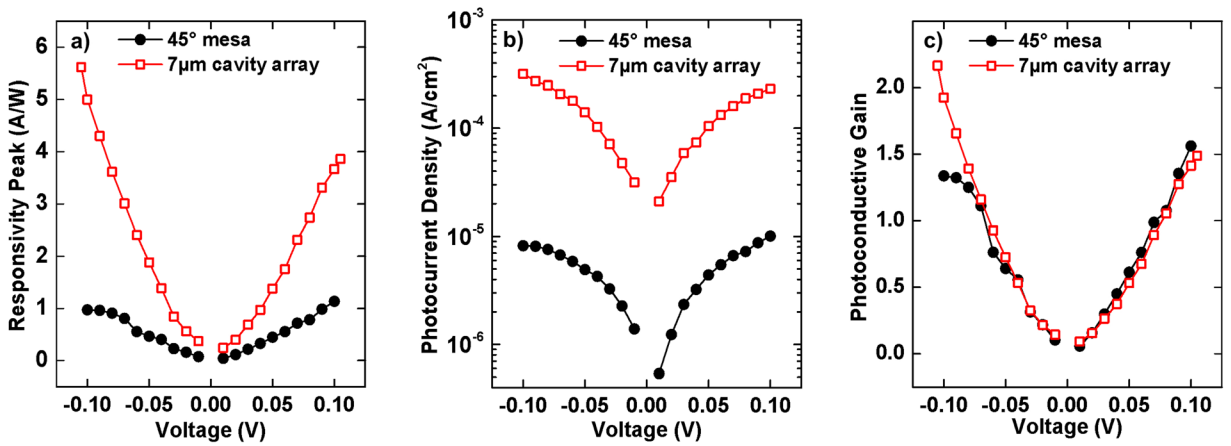

FIG. 4. (a) Responsivity peak vs voltage for the 45° mesa and the 7 μm cavity array detectors, measured with a blackbody at 500 K and QWIP temperature T = 4 K. (b) Photocurrent density vs voltage for the mesa and 7 μm cavity array detectors normalized, respectively, by the mesa area and the cavities area (where the photocurrent is generated). (c) Photoconductive spectra of the cavity array and of the 45° mesa devices, obtained by solving Eqs. (1a) and (1b), and using the measurements presented in Fig. 4(a).

TABLE I. Antenna parameters, maximum responsivity, and calculated specific detectivity. (*) indicates the measurements from the optical setup with blackbody at 500 K.

s	C	$1/Q_{cav}$	A_{isb}	$A_{isb}/(A_{isb}+1/Q_{cav})$	$R(E_{cav})$ at 0.1 V A/W	$D^*(E_{cav})$ at 0.1 V $cmHz^{1/2}/W$
6 μm	0.15	0.10	0.04	0.27	1.79	3.02×10^{12}
7 μm	0.22	0.14	0.08	0.37	3.94	5.69×10^{12}
					3.67 (*)	5.29×10^{12} (*)
8 μm	0.18	0.13	0.04	0.24	1.94	2.35×10^{12}
9 μm	0.10	0.10	0.02	0.13	0.62	0.65×10^{12}
400 μm-mesa	…	…	…	…	1.14 (*)	0.67×10^{12} (*)

summarized in Table I; as expected, the highest value $A_{isb} \approx A_{isb0} = 0.08$ is observed for the 7 μm antenna, where $E_{cav} \approx E_{21}$.

Using the measured responsivity of the $s = 7\,\mu$m detector and Eq. (1b), we calculated the corresponding gain, which is plotted in Figure 4(c) (squares). The estimated values coincide very well with those extracted for the mesa device. Indeed, the photoconductive gain is an intrinsic property of the active region, independent of the detector geometry. Moreover, this confirms the objective of our study, which is to prove that detector with the same absorbing region can be significantly improved by changing the design of the surrounding photonic structure.

THz QWIPs have similar gain to the mid-infrared detectors[8] as the gain is related to the capture probability p_c of carriers in the quantum wells.[29] From the relation $p_c = 1/(gN_{QW})$, we find $0.03 \le p_c \le 0.4$, which is consistent with that expected for a QWIP with $N_{QW} = 20$.[28]

Using our model, we have estimated the expected responsivity for all arrays, as reported in Table I. From measurements of the IV characteristics and the responsivity, we have also estimated the dark current-limited specific detectivity, defined as:[30] $D^* = R\sqrt{S_{det}}/\sqrt{4egI_{dark}}$. Using photon collection areas $S_{det} = 1.1 \times 10^5\ \mu m^2$ (mesa) and $S_{det} = 9.4 \times 10^4\ \mu m^2$ (cavity array), we obtain maximum $D^* = 5 \times 10^{12}\,cmHz^{1/2}/W$ at 4 K for the arrays, in comparison with $0.7 \times 10^{12}\,cmHz^{1/2}/W$ for the mesa device. We attribute this seven-fold improvement of D^* to the better collection efficiency of our structure, combined with the reduction of the dark current. The maximum estimated values of D^* are comparable with those of standard super-lattice detectors.[33] Another system that can be considered for comparison are commercially available doped Ge bolometers with optical NEP (Noise Equivalent Power) = 2.2 $pW/Hz^{1/2}$ from a collection area $S_{det} = 2.5 \times 10^7\ \mu m^2$.[34] This corresponds to a background-limited detectivity[30] $D^*_{BL} = 2.2 \times 10^{11}\,cmHz^{1/2}/W$. For the device showing the highest performance in this paper, the 7 μm patch antenna, we estimate very similar values: $D^*_{BL} = 1.7 \times 10^{11}\,cmHz^{1/2}/W$ and an optical NEP = 0.18 $pW/Hz^{1/2}$. Furthermore, in our system, there is still room for improvement as the absorbing area can be further reduced with respect to the photon collection area,[20] while the contrast C could be adjusted to 1.[22]

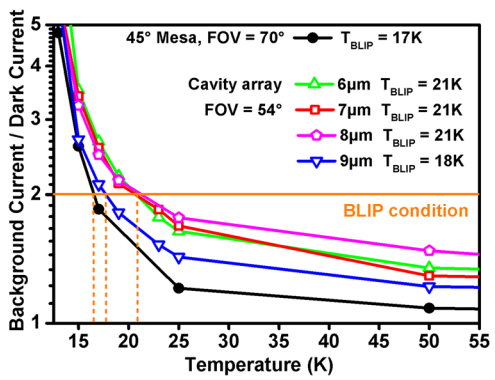

FIG. 5. The ratio of the background and dark currents measured at optimum voltage for the cavity array devices and for the 45° mesa device. The background current is $I_{background} = I_{photo} + I_{dark}$, where I_{photo} is the photocurrent generated by a 300 K background with the indicated FOVs.

Another benefit of the reduction of the dark current in the patch antenna array geometry is an improved BLIP (background limited infrared photodetector) performance. This effect is illustrated in Figure 5, where the ratio $I_{background}/I_{dark}$[19] is plotted as a function of the detector temperature. Since this ratio generally depends on the applied bias, for each structure we have plotted the maximum ratio $I_{background}/I_{dark}$, which was obtained in the voltage range 0.05–0.075 V. The BLIP temperature T_{BLIP} is defined such as $I_{background}/I_{dark} = 2$; under this condition, the photocurrent generated by the background is exactly equal to the detector dark current.[30] From Figure 5, it can be clearly seen that the antenna devices show better thermal behavior than the 45° mesa detector, with $T_{BLIP} = 21$ K registered for the 6–7–8 μm antennas with a FOV = 54°, in comparison with the BLIP, $T_{BLIP} = 17$ K of the mesa with a FOV = 70°, the results for the antenna devices are higher than previously reported values.[8,17] It is also notable from Figure 5 that for the $s = 8\,\mu$m device the photocurrent $I_{photo} = I_{background} - I_{dark}$ remains an important fraction (33%) of the total current even at temperatures as high as 50 K.

In summary, we implemented a THz QWIP absorbing region in a patch antenna array geometry. By comparing the cavity array devices with a 45° polished mesa, made of the same absorbing region, we clearly reveal the advantages of our plasmonic structure in terms of a higher responsivity and a better thermal performance of the detectors. Furthermore, we estimate the dark-current limited detectivity D^* to be as high as $5 \times 10^{12}\,cmHz^{1/2}/W$ and with a background limited detectivity $D^*_{BL} = 1.7 \times 10^{11}\,cmHz^{1/2}/W$ at 4 K and 5.4 THz. While these values are still to be confirmed by noise measurements, we believe that our geometry allows THz frequency QWIPs to perform comparably with commercially available THz photodetectors.

We acknowledge financial support from ERC projects "Adequate" and "TOSCA," and ANR-11-IDEX-0005-02

(Labex SEAM Project "Capture"). We also acknowledge support of the EPSRC, the Royal Society and the Wolfson Foundation. D.P. would like to acknowledge support through the FP7 ITN NOTEDEV network.

[1]M. Tonouchi, Nat. Photonics **1**(2), 97 (2007).
[2]B. Ferguson and X. C. Zhang, Nat. Mater. **1**, 26 (2002).
[3]R. Köhler, A. Tredicucci, F. Beltram, H. E. Beere, E. H. Linfield, A. G. Davies, D. A. Ritchie, R. C. Iotti, and F. Rossi, Nature **417**, 156 (2002).
[4]C. Sirtori, S. Barbieri, and R. Colombelli, Nat. Photonics **7**, 691 (2013).
[5]S. Barbieri, P. Gellie, G. Santarelli, L. Ding, W. Maineult, C. Sirtori, R. Colombelli, H. Beere, and D. Ritchie, Nat. Photonics **4**(9), 636 (2010).
[6]A. Rogalski and F. Sizov, Opto-Electron. Rev. **19**(3), 346 (2011).
[7]G. N. Gol'tsman, Infrared Phys. Technol. **40**, 199 (1999).
[8]H. Luo, H. C. Liu, C. Y. Song, and Z. R. Wasilewski, Appl. Phys. Lett. **86**, 231103 (2005).
[9]X. G. Guo, Z. Y. Tan, J. C. Cao, and H. C. Liu, Appl. Phys. Lett. **94**, 201101 (2009).
[10]J. C. Cao and H. C. Liu, Semicond. Semimetals **84**, 195 (2011).
[11]M. Graf, G. Scalari, D. Hofstetter, J. Faist, H. Beere, E. Linfield, D. Ritchie, and G. Davies, Appl. Phys. Lett. **84**, 475 (2004).
[12]M. Patrashin, I. Hosako, and P. Merken, Proc. SPIE **6038**, 60380H (2006).
[13]M. Patrashin and I. Hosako, Opt. Lett. **33**, 168 (2008).
[14]B. F. Levine, K. K. Choi, C. G. Bethea, J. Walker, and R. J. Malik, Appl. Phys. Lett. **50**, 1092 (1987).
[15]M. Helm, *The Basic Physics of Intersubband Transitions*, edited by H. C. Liu and F. Capasso (Academic Press, San Diego, 2000).
[16]R. Zhang, Z. L. Fu, L. L. Gu, X. G. Guo, and J. C. Cao, Appl. Phys. Lett. **105**, 231123 (2014).
[17]L. L. Gu, R. Zhang, Z. Y. Tan, W. J. Wan, R. Yin, X. G. Guo, and J. C. Cao, J. Phys. D: Appl. Phys. **47**, 165101 (2014).
[18]A. Benz, M. Krall, S. Schwarz, D. Dietze, H. Detz, A. M. Andrews, W. Schrenk, G. Strasser, and K. Unterrainer, Sci. Rep. **4**, 4269 (2014).
[19]Y. N. Chen, Y. Todorov, B. Askenazi, A. Vasanelli, G. Biasiol, R. Colombelli, and C. Sirtori, Appl. Phys. Lett. **104**, 031113 (2014).
[20]C. Feuillet-Palma, Y. Todorov, A. Vasanelli, and C. Sirtori, Sci. Rep. **3**, 1361 (2013).
[21]C. A. Balanis, *Antenna Theory* (John Wiley & Sons, 2005).
[22]Y. Todorov, L. Tosetto, J. Teissier, A. Andrews, P. Klang, R. Colombelli, I. Sagnes, G. Strasser, and C. Sirtori, Opt. Express **18**, 13886 (2010).
[23]Y. Todorov, A. M. Andrews, I. Sagnes, R. Colombelli, P. Klang, G. Strasser, and C. Sirtori, Phys. Rev. Lett. **102**, 186402 (2009).
[24]A. Gomez, V. Berger, N. Pere-Laperne, and L. De Vaulchier, Appl. Phys. Lett. **92**, 202110 (2008).
[25]A. Delga, L. Doyennette, A. Buffaz, V. Berger, F. R. Jasnot, L. A. de Vaulchier, N. Péré-Laperne, and H. C. Liu, J. Appl. Phys. **110**, 013714 (2011).
[26]C. Kittel, *Introduction to Solid State Physics*, 7th ed. (John Wiley & Sons, 1996).
[27]A. Zussman, B. F. Levine, J. M. Kuo, and J. de Jong, J. Appl. Phys. **70**, 5101 (1991).
[28]H. C. Liu, *Intersubband Transitions in Quantum Wells: Physics and Device Applications*, edited by H. C. Liu and F. Capasso (Academic Press, San Diego, 2000).
[29]H. C. Liu, Appl. Phys. Lett. **60**, 1507 (1992).
[30]E. Rosencher and B. Vinter, *Optoelectronics* (Cambridge University Press, 2004).
[31]T. Ando, A. B. Fowler, and F. Stern, Rev. Mod. Phys. **54**, 437 (1982).
[32]G. Pegolotti, A. Vasanelli, Y. Todorov, and C. Sirtori, Phys. Rev. B **90**, 035305 (2014).
[33]T. Ueda, Z. An, and S. Komiyama, J. Infrared, Millimeter, Terahertz Waves **32**(5), 673 (2010).
[34]See http://www.terahertz.co.uk for technical data on commercial Ge bolometers, (accessed 2 March 2015).